Journal of Water Process Engineering 56 (2023) 104432

Contents lists available at ScienceDirect

Journal of Water Process Engineering

journal homepage: www.elsevier.com/locate/jwpe

High perm-selectivity and performance of tuned nanofiltration membranes by merging carbon nitride derivatives as interphase layer for efficient water treatment

Sadegh Aghapour Aktij [a,b], Milad Hosseininejad [c], Mostafa Dadashi Firouzjaei [d], Saeed Farhadi [c], Mark Elliott [d], Ahmad Rahimpour [b,*], João B.P. Soares [a,*], Mohtada Sadrzadeh [b,*], Yaghoub Mansourpanah [c,*]

[a] *Department of Chemical & Materials Engineering, 12-263 Donadeo Innovation Centre for Engineering, Group of Applied Macromolecular Engineering, University of Alberta, Edmonton T6G 1H9, AB, Canada*
[b] *Department of Mechanical Engineering, 10-367 Donadeo Innovation Center for Engineering, Advanced Water Research Lab (AWRL), University of Alberta, Edmonton T6G 1H9, AB, Canada*
[c] *Membrane Research Laboratory, Lorestan University, Khorramabad 68151-44316, Iran*
[d] *Department of Civil, Construction and Environmental Engineering, University of Alabama, Tuscaloosa, AL, USA*

ARTICLE INFO

Keywords:
Interlayered thin film nanocomposite membranes
Polyamide
Interfacial polymerization
Fouling mitigation
Separation

ABSTRACT

The support characteristics under polyamide thin films have proven significant impact on the performance of nanofiltration thin film composite (TFC) membranes. In this study, polyethersulphone (PES) support was initially furnished with an interphase layer of different graphitic carbon nitride derivatives and nanocomposites ($g\text{-}C_3N_4$, oxidized $g\text{-}C_3N_4$, and $g\text{-}C_3N_4/CuFe_2O_4$) to improve the specifications of TFC membranes. Then, the polyamide layer was fabricated by interfacial polymerization on top of the interphase layer. The interlayer helped fine-tune the thickness and surface characteristics such as roughness, wettability, and zeta potential of the polyamide layer, in the way of improving the separation and antifouling capabilities of the TFC membranes. The interlayered thin film nanocomposite (ITFN) membranes considerably indicated better water permeability and rejection of methylene blue (MB), methyl orange (MO), Cadmium nitrate, and sodium sulfate (Na_2SO_4). We showed that ITFNs loaded with 0.01 wt% $g\text{-}C_3N_4/CuFe_2O_4$ had a permeability of ~9.2 LMH/bar, upper from ~3.8 LMH/bar in the pristine form, exhibiting outstanding water flux. The rejection data showed nearly two-fold increase of rejection of Cadmium nitrate, sodium sulfate, and dyes rather than the pristine nanofiltration membrane. The modified nanofiltration membranes remarkably exhibited better antifouling properties and higher flux recovery ratios as well.

1. Introduction

Many industrial processes release wastewater tainted with salts, dyes, and heavy metal ions to the environment [1]. These pollutants must be removed from wastewater because they are toxic, carcinogenic, and teratogenic in low quantities [2]. One of the most effective ways to achieve this objective is to use membranes [3,4]. Compared to conventional chemical or physical methods, nanofiltration (NF) has garnered significant interest for water treatment because it is easy to operate and scale-up, consumes little energy, and has high separation efficiency [5,6].

Thin film composite (TFC) polyamide membranes are good candidates for nanofiltration processes because they combine mechanical stability, low cost, and simple manufacture [7], but they are not without limitations [8]. The heterogeneity of the polyamide layer and membrane fouling adversely affect the performance and lifetime of TFC membranes [9]. Recently, applying functional interlayers onto the substrate has been demonstrated to enhance the performance of TFC membranes. The interlayer prevents the polyamide layer from intrusion into the porous substrate and modifies its morphology, mainly by decreasing the

---

* Corresponding authors.
E-mail addresses: arahimpo@ualberta.ca (A. Rahimpour), jsoares@ualberta.ca (J.B.P. Soares), sadrzade@ualberta.ca (M. Sadrzadeh), mansourpanah.y@lu.ac.ir (Y. Mansourpanah).

https://doi.org/10.1016/j.jwpe.2023.104432
Received 17 July 2023; Received in revised form 2 October 2023; Accepted 13 October 2023

thickness and surface roughness of the polyamide layer [10]. Incredibly, support selection is no longer restricted by factors such as hydrophilicity, pore size, or surface uniformity when it can be modified with an interlayer having the desired nanostructure [11,12]. Functional interlayers aid in the creation of polyamide selective layers by enhancing amine storage at the interface, regulating amine diffusion, interfering with heat and nano-bubble generation, as well as controlling the formation of nuclei [13].

Two-dimensional (2D) nanosheets, such as graphene oxide (GO) [11,14], metal-organic frameworks (MOF) [15,16], and covalent organic frameworks (COFs) [17] can be used to make uniform and continuous interlayers for interlayered thin film nanocomposite (ITFN) membranes [18]. ITFN acronym was used by Mansourpanah for the first time to describe the nanoparticle-based interphased and interlayered thin film nanocomposite membranes [18]. Unfortunately, GO-, MOF-, and COF-based membranes are sensitive to water [14]. This has limited their applications and commercialization because water is present in most liquid separation processes.

Graphitic carbon nitride (g-C_3N_4) is a novel 2D nanomaterial with tri-*s*-triazine structural units and a wide variety of desirable characteristics [2,19], such as low cost, straightforward synthesis, excellent mechanical, thermal, and chemical stability, photodegradability, easy aqueous dispersion, and environmental friendliness [2]. The tri-*s*-triazine structural unit comprises 6-membered rings containing sp^2-hybridized C and N atoms that can form an aromatic p-conjugated structure [7]. Its structure makes g-C_3N_4 thermochemically stable in alkaline and acidic environments [2]. The interlayer spacing in g-C_3N_4 is mainly created by unstripped fragments attached to the nanosheets, serving as a highly permeable gutter layer with additional water channels [20]. Chemically inert and mechanically rigid, these fragments act as self-supporting spacers between the g-C_3N_4 nanosheets. While numerous 2D nanosheet-based membranes, including GO, MOF, and COF, may display sensitivity to water, leading to swelling and alterations in selectivity that restrict their extensive applications in aquatic-based liquid separation processes, the g-C_3N_4 interlayered membrane remains stable even in such conditions [14].

While recent studies have explored the use of g-C_3N_4 to enhance the performance of TFC membranes, either as a hydrophilic additive in amine solutions [16,17] or as interlayers [21–23], the unique approach of employing different graphitic carbon nitride derivatives and nanocomposite as interlayers in TFC membranes sets our work apart. In this work, g-C_3N_4, oxidized g-C_3N_4 (g-C_3N_4-Ox), and g-C_3N_4/$CuFe_2O_4$ nanocomposite were synthesized and used as interlayers of TFC nanofiltration membranes for removing dyes, heavy metal ions, and salts. First, g-C_3N_4 was prepared by thermal decomposition of urea. After being exfoliated, g-C_3N_4 was chemically oxidized to form g-C_3N_4-Ox nanosheets, resulting in oxygen-containing functional groups (carboxyl and hydroxyl groups) on their basal planes to escalate the hydrophilicity. Finally, the synthesized g-C_3N_4-Ox nanosheets were decorated onto copper ferrite, $CuFe_2O_4$ (CFO), via a facile hydrothermal method to make a novel g-C_3N_4-CFO nanocomposite that performed better than the previous materials. The chemical composition and surface morphologies of ITFN membranes made with several g-C_3N_4 nanosheet contents were analyzed. The performance and antifouling properties of the fabricated membranes were then comprehensively assessed.

2. Materials and methods

2.1. Materials and chemicals

All chemicals employed in this research were utilized in their received state. Urea ($CO(NH_2)_2$, ≥ 99 %) as a precursor of g-C_3N_4, 2-propanol (IPA, C_3H_8O, >99.8 %), ethanol (EtOH, C_2H_6O, >98 %), Copper (II) chloride ($CuCl_2$), sodium hydroxide (NaOH), ammonium iron(III) sulfate dodecahydrate($(NH_4)Fe(SO_4)_2 0.12H_2O$), copper(II) sulfate pentahydrate ($CuSO_4 0.5H_2O$), nitric acid (HNO_3, 65 %), hydrogen peroxide (H_2O_2, 30 %), and acetone were bought from Merck. Polyethersulfone pellets (PES, Solvay, M_w = 62 kDa–64 kDa), polyvinylpyrrolidone (PVP, Sigma-Aldrich, M_w = 10 kDa), Triton X-100 (Merck), and *N*, *N*-Dimethylformamide (DMF, Sigma-Aldrich, 99.8 %) were used to make the PES support. Piperazine (PIP, 99 %, Acros Organics) and trimesoyl chloride (TMC, 98 %, Acros Organics) were

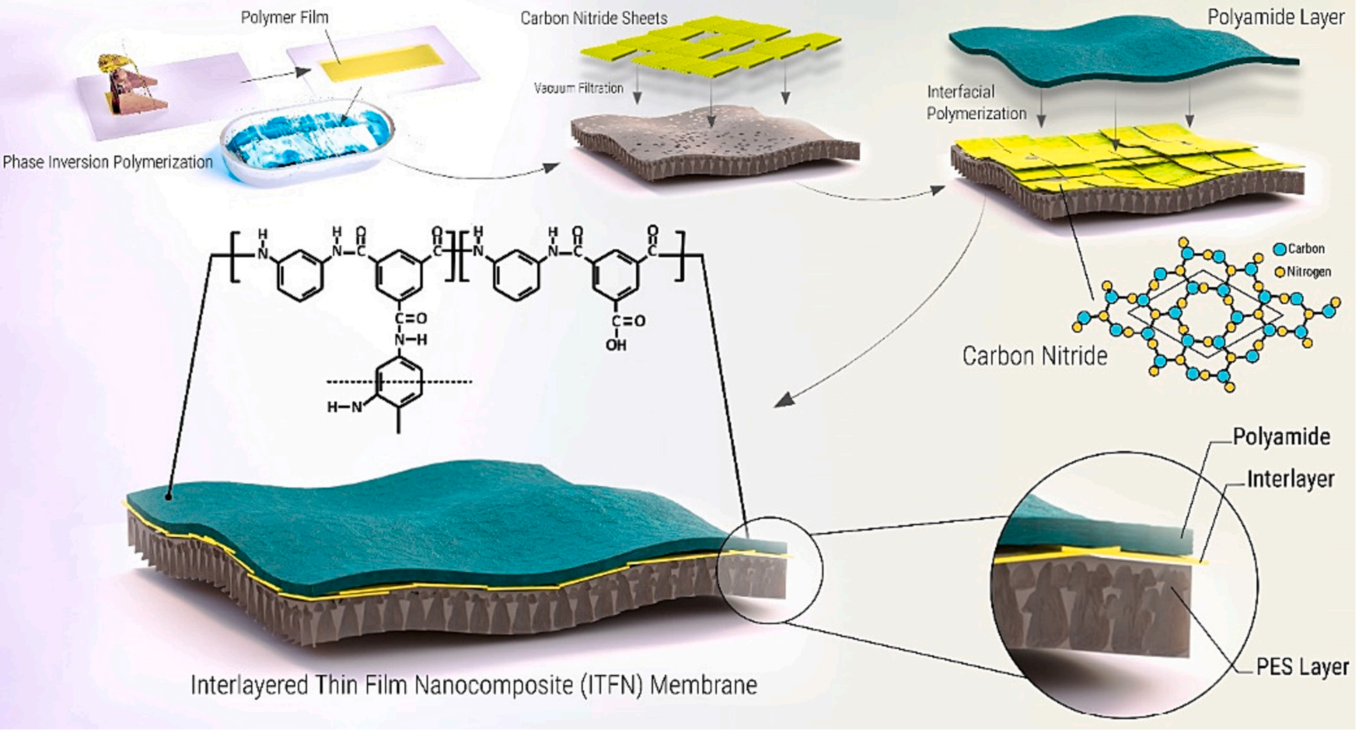

Fig. 1. Schematic illustration of the membrane fabrication steps and high magnification cross-sectional illustration of the prepared ITFN membrane.

employed as the active monomers for the synthesis of the polyamide selective layer on the PES support surface. The effectiveness of the fabricated TFC membranes in removing salt, heavy metal, and dye was assessed by evaluating their separation performance using feed solutions of sodium sulfate (Na_2SO_4) at 1000 ppm, Cadmium nitrate ($Cd(NO_3)_2.4H_2O$, Sigma-Aldrich) at 20 ppm, the cationic dye methylene blue (Sigma-Aldrich, Mw = 319.8 Da) at 50 ppm, and the anionic methyl orange (Sigma-Aldrich, Mw = 327.3 Da) at 50 ppm.

2.2. *Preparation of g-C_3N_4 (CN) nanosheets*

The g-C_3N_4 was synthesized by thermal decomposition of urea [17,24], in which 10 g was loaded into a loosely covered ceramic crucible after complete grinding by mortar and pestle. The crucible was subjected to a gradual temperature increase in a furnace, starting from 23 °C and reaching 550 °C over a period of 2 h, with a heating rate of 9 °C per minute. Once cooled to ambient temperature, the resulting yellow powder underwent three rounds of washing using nitric acid (0.1 M) and deionized water to effectively eliminate any impurities present. Ultimately, the filtrate was subjected to drying at 60 °C for a duration of 12 h, denoted as CN. The product yield from this synthesis process was determined to be 0.42 g-C_3N_4 g/10 g urea.

2.3. *Preparation of g-C_3N_4-Ox (CNOx) nanosheets*

A mass of 2 g of CN was added into a 40 solution of sulfuric acid and nitric acid (1:1) and heated at 40 °C *with* 2 h sonication. After adding H_2O_2 (33 %) dropwise to the mixture, it was sonicated for 3 h for exfoliation. Once the suspension achieved a yellow product, it was diluted by adding 150 ml of deionized water. Subsequently, the diluted suspension was subjected to centrifugation at a speed of 10,000 rpm for a duration of 10 min. In the next step, oxidized CN (g-C_3N_4-Ox) was washed alternately with DI water and acetone, and dried overnight at 70 °C, resulting in yellow exfoliated g-C_3N_4-Ox sheets with a product yield of 1.7 g g-C_3N_4-Ox/2 g g-C_3N_4, denoted as CNOx.

2.4. *Preparation of g-C_3N_4/$CuFe_2O_4$ (CNCFO) nanocomposite*

g-C_3N_4/$CuFe_2O_4$ nanocomposite was synthesized using a facile hydrothermal method according to the literature [25]. A mass of 60 mg of CN was dispersed in 30 ml of distilled water under sonication for 2 h, followed by 1 mmol of $CuSO_40.5H_2O$, and 2 mmol of $(NH_4)Fe(SO_4)_20.12H_2O$ were added to another 30 ml of distilled water, after which two solutions mixed by 30 min stirring. Next, 20 mL of a solution containing 20 mmol of NaOH was added dropwise to the previous mixture under 30-minute vigorous stirring. The solution was then placed in a stainless-steel autoclave and allowed to react for 14 h at 140 °C. Finally, After the product had cooled down to room temperature, it underwent multiple washings using deionized water and ethanol, followed by drying at a temperature of 60 °C, denoted as CNCFO. This synthesis process yielded 215 mg of the CNCFO nanocomposite.

2.5. *Thin-film membranes fabrication*

PES ultrafiltration membranes, fabricated via non-solvent-induced phase separation (NIPS), were used as substrates [26,27]. A vacuum filtration method was used to construct g-C_3N_4 interlayers [28–30], followed by interfacial polymerization to fabricate all ITFN polyamide membranes, as shown in Fig. 1. CN, CNOx, and CNCFO aqueous suspensions with different mass concentrations (0.0012 wt/v%, 0.0025 wt/v%, 0.01 wt/v%) were prepared by dispersing into DI water. Following 30 min of sonication, the 10 mL of selected aqueous suspensions were transferred into a funnel and filtered onto a PES membrane coupon with a filtration area of 9 cm^2, utilizing vacuum filtration at a pressure of 0.2 bar. Coated PES membranes were prepared with material loadings of 13.33, 27.78, and 111.11 $\mu g \cdot cm^{-2}$ for mass concentrations of 0.0012 wt/v%, 0.0025 wt/v%, and 0.01 wt/v%, respectively.

Table 1
The summary of membranes' labeling and structure information.

Membrane name	Interlayer	2D materials (wt/v%)
TFC-0	✘	0
ITFN-CN-12	✓	0.0012
ITFN-CN-25	✓	0.0025
ITFN-CN-100	✓	0.0100
ITFN-CNOx-12	✓	0.0012
ITFN-CNOx-25	✓	0.0025
ITFN-CNOx-100	✓	0.0100
ITFN-CNCFO-12	✓	0.0012
ITFN-CNCFO-25	✓	0.0025
ITFN-CNCFO-100	✓	0.0100

To prepare ITFNs, 10 ml of the aqueous solution containing 2 wt% PIP was poured onto the surface of the pre-coated membrane. After a contact time of 2 min, the solution was drained off. Then, an air knife was utilized to remove any excess aqueous solution present on the upper surface of the membrane. Afterward, the membrane surface was coated with 5 mL of a 0.2 wt/v% TMC in n-hexane solution, allowing it to remain for 1 min to facilitate the completion of the polymerization reaction. After forming the selective layer, the membrane was cured in an oven at 70 °C for 30 min. The resultant ITFN membranes were labelled according to the interlayer type (X; CN, CNOx, CNCFO) and loading (Y; 12, 25, and 100 for 0.0012 wt/v%, 0.0025 wt/v%, and 0.0100 wt/v%, respectively): ITFN-X-Y. TFC-0 stands for the control TFC membrane prepared on the pristine PES support without an interlayer. Table 1 summarizes the membranes labeling procedure. Detailed information regarding the physiochemical characterization, experimental procedures for NF filtration, and fouling experiments conducted on the fabricated membranes are provided in the Supporting Information.

2.6. *Performance evaluation of the membranes*

A bench-scale dead-end stirred cell with a cell volume of 80 mL and an effective membrane area of 5 cm^2 was used for the filtration tests (flux, solute rejection, and fouling) of the prepared membranes. All experiments were done at a constant transmembrane pressure (TMP) of 3 bar using a nitrogen cylinder under continuous stirring at 400 rpm to minimize concentration polarization. Pure water was passed through the membrane for one to two hours to pre-compact it until the flux stabilized at a value that remained constant for over half an hour. For each membrane, the pure water permeability (PWP) was determined by collecting the permeate over 5 min in a parafilm-covered glass beaker. The pure water flux was calculated as [31]:

$$J_w = \frac{m}{A\Delta t} \tag{1}$$

where J_w ($L\ m^{-2}h^{-1}$; LMH) is the pure water flux, m (kg) is the weight of the permeated water, A (m^2) is the active surface area of the membrane, and Δt (h) is the operating time. After measuring the pure water flux, foulant/solute solutions, including dyes (MB and MO), heavy metal (Cd^{2+}), and salt (Na_2SO_4) were filtered, and a sample of ~3 mL was collected when the filtrate color had stabilized after at least an hour of equilibrium. Samples collected from the feed and permeated water were analyzed using a conductometer (JENWAY 4510), UV–vis spectrophotometer (Shimadzu1650PC), and atomic absorption spectrometer (Shimadzu AA-670) according to the nature of the solute.

The membranes' separation performance was assessed by determining the percentage rejection of the feed components, which was calculated as follows [4,8]:

$$R(\%) = 1 - \frac{C_p}{C_f} \times 100 \tag{2}$$

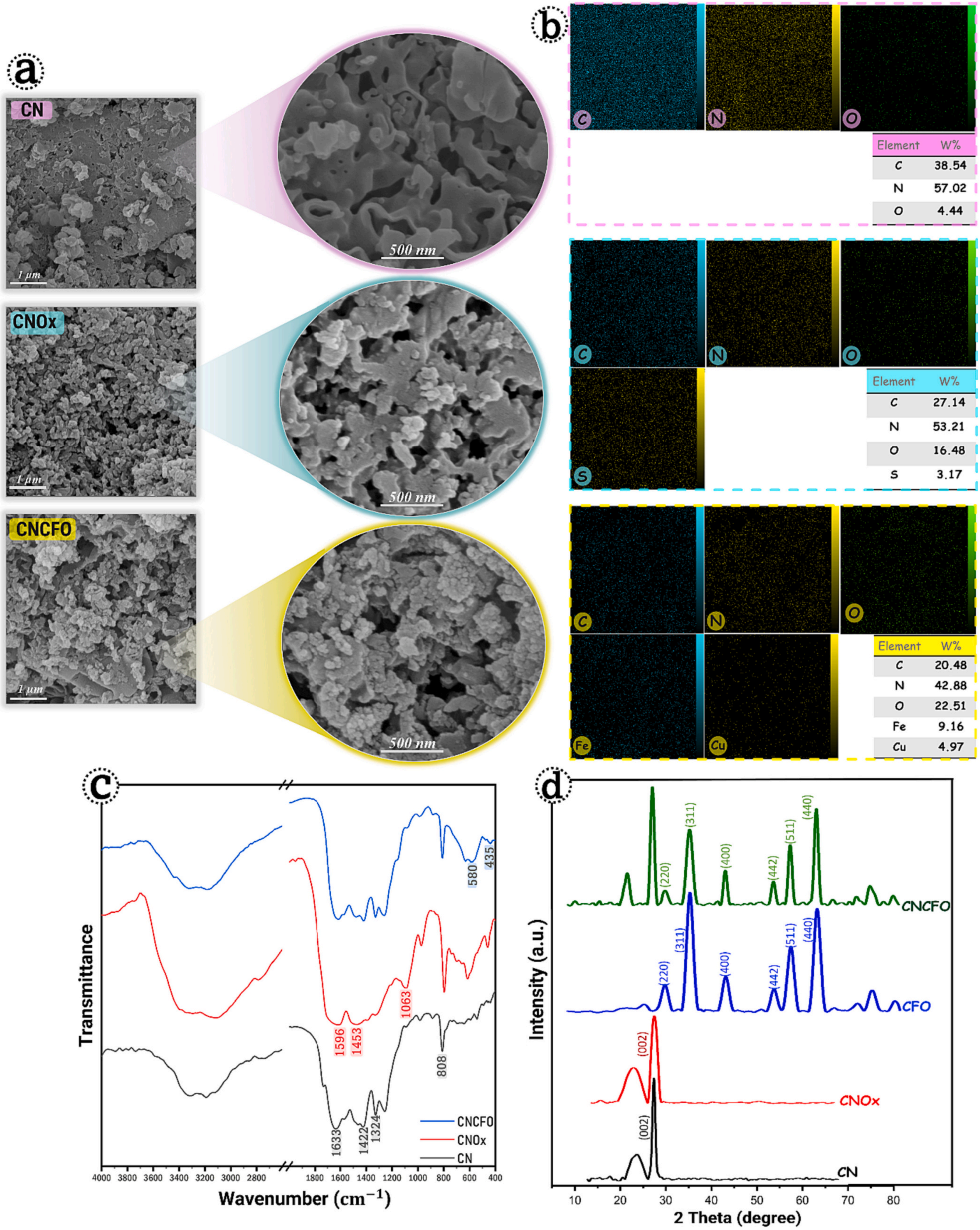

Fig. 2. SEM images (a), EDX mapping (b), FTIR (c), and XRD patterns (d) of CN, CNOx, and CNCFO nanosheets.

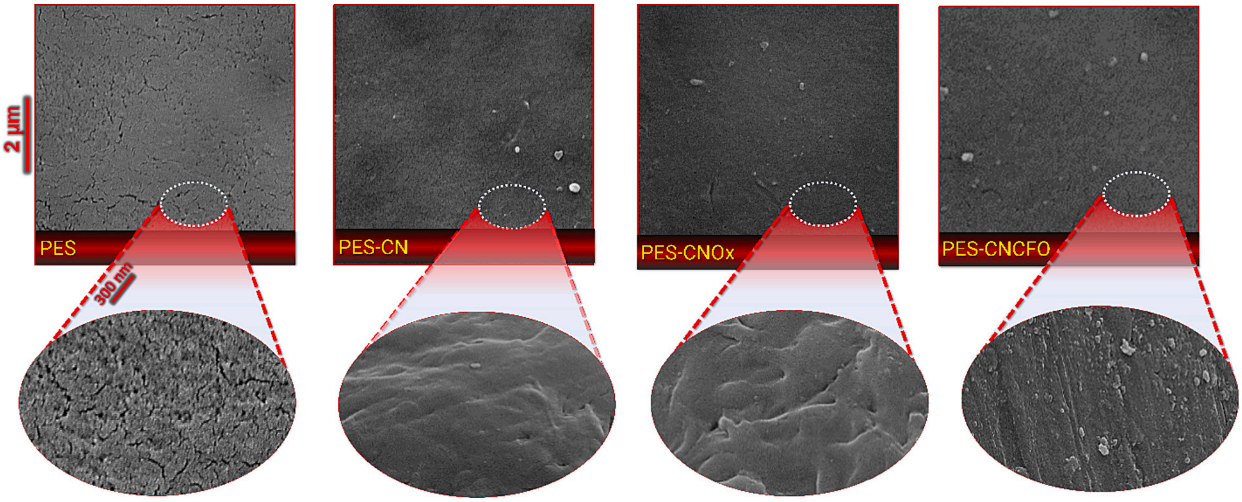

Fig. 3. Surface SEM images of the PES substrate with 0.0025 wt/v% loading and without nanosheet coating.

where C_p and C_f are the concentrations of the permeate and feed, respectively. The investigation of membrane fouling characteristics aimed to evaluate the antifouling properties of TFC-0 and ITFN membranes. A model foulant solution was prepared by dissolving 100 mg of BSA in 1 L of deionized water to achieve a concentration of 100 ppm, serving as a representative foulant for this assessment. The antifouling experiment was structured into three distinct steps. Initially, the pure water flux through the membrane, denoted as J_{w1} (LMH), was measured at a TMP of 3 bar for 1 h, establishing a baseline for membrane performance before fouling. Subsequently, the model foulant solution was introduced into the nanofiltration system, and the flux, denoted as J_v (LMH), was recorded under a consistent TMP of 3 bar for a duration of 2 h, simulating a fouling scenario. Following the fouling phase, a cleaning regimen was employed where the fouled membrane was rinsed with pure water at a controlled temperature of 27 ± 1 °C for 10 min to dislodge the adhered foulants. Post cleaning, the pure water flux of the cleaned membrane, denoted as J_{w2} (LMH), was measured again at a TMP of 3 bar to evaluate the recovery of membrane performance. Multiple indices were employed to assess the membranes' antifouling capabilities, such as the flux recovery ratio (FRR), the flux loss caused by reversible fouling resistance (R_r), the flux loss caused by irreversible fouling resistance (R_{ir}), and the total flux decline ratio (R_t). These indices are defined in the following equations [32,33]:

$$\mathrm{FRR}(\%) = \left(\frac{J_{w2}}{J_{w1}}\right) \times 100 \tag{3}$$

$$R_r(\%) = \left(\frac{J_{w2} - J_v}{J_{w1}}\right) \times 100 \tag{4}$$

$$R_{ir}(\%) = \left(\frac{J_{w1} - J_{w2}}{J_{w1}}\right) \times 100 \tag{5}$$

$$R_t(\%) = R_r + R_{ir} = \left(\frac{J_{w1} - J_v}{J_{w1}}\right) \times 100 \tag{6}$$

3. Results and discussions

3.1. Structure and surface properties of synthesized nanosheets

The morphologies of CN, CNOx, and CNCFO samples – measured by SEM – are shown in Fig. 2a. CN has a distinctive lamellar structure [34]. The morphology of CNOx was similar to that of CN, with a wide variety of nonuniform sheet sizes, perhaps caused by stacking effects between layers and hydrogen bonding interactions mediated by oxygen-containing groups (OH, COOH, CO) [34]. CNCFO appears as platelet-like sheets with layered and curved morphologies [35]. According to EDX and elemental mapping images (Fig. 2b), the CN nanosheets are made up of C and N in almost 3:4 atomic ratios without additional impurities. Oxygen was found in the elemental analysis of the CNOx nanosheets, showing that it was effectively oxidized using the method described above. The corresponding elemental maps for CNCFO prove that C, N, Fe, Cu, and O are homogeneously distributed on the entire area of the sample. The FTIR spectra of CN, CNOx, and CNFO are compared in Fig. 2c. The large peak between 3400 and 3000 $\mathrm{cm^{-1}}$ for the CN sample corresponds to the stretching vibrations of the primary and secondary amine groups, as well as to H_2O molecules adsorbed from the atmosphere. Oxygen-containing functional groups placed onto modified g-C_3N_4 nanosheets result in more distinct peaks for CNOx and CNCFO [36]. The peak at 808 $\mathrm{cm^{-1}}$ is characteristic for tri-*s*-triazine units; it can be seen in all three samples [37]. C—N stretching of aromatic rings accounts for the peaks between 1450 and 1220 $\mathrm{cm^{-1}}$, while the peak at 1633 $\mathrm{cm^{-1}}$ results from the stretching vibrations of C═N bonds [38,39]. The peaks at 1063, 1453, and 1596 $\mathrm{cm^{-1}}$ in the spectrum of CNOx correspond to C—O, OH, and N—O functional groups, respectively [40]. The peak observed at 615 $\mathrm{cm^{-1}}$ can be attributed to the H in NH groups bridging the heptazine units, further validating the presence of these units in synthesized nanosheets [41,42]. It has been observed that the peaks in around 1400 $\mathrm{cm^{-1}}$ are attributed to the stretching of tertiary C–OH groups, suggesting the presence of O-containing substances within the range of aromatic C—N stretching [43,44]. In the FTIR spectrum of CNCFO, the peaks at 580 $\mathrm{cm^{-1}}$ and 435 $\mathrm{cm^{-1}}$ are attributed to metal-oxygen (Fe—O) bonds and the vibration of metal ions at the octahedral sites in CFO, respectively [25,45].

The crystalline structure of the nanoparticles was analyzed by comparing XRD patterns of CN, CNOx, and CNCFO (Fig. 2d). The diffraction patterns for CN and CNCFO agree with those reported in the literature [36,46]. The sharp peak at $2\Theta = 27.3^\circ$ is associated with the (002) plane and is ascribed to tri-*s*-triazine interlayer stacking reflections, demonstrating that CN was successfully synthesized [46]. For CNOx, a slight broadening of the (002) peak, relative to CN, suggests a decrease in crystallite size, potentially due to the oxidation process [47]. Additionally, the reduced peak intensity in CNOx, in comparison to CN, indicates a decrease in crystallinity, which can be attributed to the introduction of oxygen-containing functional groups during the oxidation process [48]. Furthermore, there is a slight shift in the (002) peak from 27.3° to 27.5° for CNOx, which is an indicative of a change in the interlayer spacing [49,50]. This shift can be attributed to the denser packing of the oxidized layers, a result of enhanced π–π stacking and

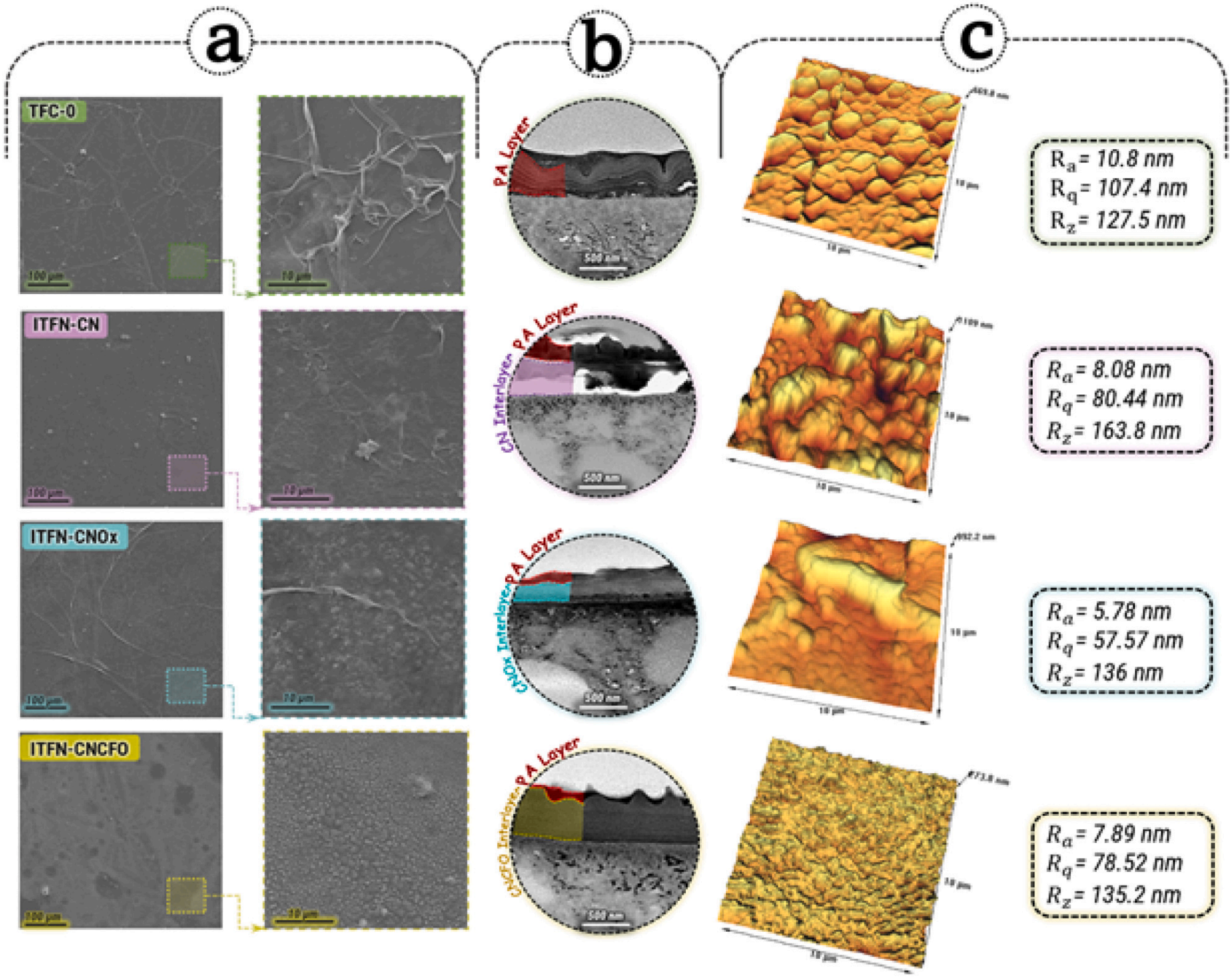

Fig. 4. FESEM (a), TEM (b), AFM 3D images, and surface roughness parameters (c) of the fabricated membranes.

hydrogen bonding interactions [35,51]. It was also found that hybridization with CN did not affect the XRD pattern of CFO. The distinct peaks identified around 30, 35, 43, 53, 57, and 62 for the pure CFO sample align with the planes (220), (311), (400), (442), (511), indicating that CFCN was synthesized as a two-phased composite.

3.2. Morphology of the membranes

The surface morphologies of the PES substrate with 0.0025 wt/v% loading and without a nanosheet coating are contrasted in Fig. 3. The absence of visible pores on the PES substrate suggests a successful and homogeneous formation of a thin interlayer on top of the substrates. More specifically, the pores of the PES substrate are covered and replaced by smaller stacking pores formed by the nanosheets, which subsequently facilitate enhanced control over the reaction-diffusion process during the interfacial polymerization (IP) reaction. The membrane surface exhibits a smooth layer after being coated with suspensions containing CN, CNOx, and CNCFO nanosheets. Notably, the CNCFO-coated sample demonstrates a rougher surface compared to the CN and CNOx-coated substrates, attributable to the inherent wrinkled structure of CNCFO itself [52]. Fig. 4a and b reveal FESEM and TEM images respectively, providing visual evidence for the successful formation of the polyamide active layer on the PES support that was modified with various interlayers. The ITFN membranes, as shown in the cross-sectional TEM image, are made up of three layers: a polyamide outer layer, a nanosheet interlayer, and a PES substrate. During interfacial polymerization, the polyamide layer in the TFC-0 membrane (without a nanosheet interlayer) presents stripe structure of conventional nanofiltration membranes [53]. This structure is likely due to the diffusion of PIP towards the interface of the organic solution during the polymerization process [4]. In contrast, ITFN membranes display less pronounced surface features. Furthermore, in the case of the ITFN-CNCFO membrane, the polyamide stripe formations appear to be flattened, resulting in a more nodular structure. The polyamide layer of the TFC-0 membrane was around 250 nm thick, while the thickness of ITFN-CN, ITFN-CNOx, and ITFN-CNCFO membranes were around 160, 95, and 110 nm, respectively. Because the polyamide layer is formed by a mechanism of self-limited diffusion control, variations in the PIP diffusion rate affect the membrane thickness [54]. According to Zhang et al. [55], the hydrophilic interlayer containing PVA and GO nanosheets – with plenty of hydroxyl groups – affect the diffusion rate of PIP molecules to the membrane interface due to hydrogen bonding with the amine groups. Liu et al. [56] suggested that hydrogen bond interactions with poly(amidoxime) interlayers slowed the diffusion of the PIP molecules to the interface with the organic phase, leading to the formation of a thinner skin layer that allowed for higher filtration fluxes. Similarly, the CN nanosheets have several reactive amino groups, which may interact with the diffusing PIP via electrostatic forces and hydrogen bonds. This may reduce the PIP diffusion rate. To facilitate the regulated release of PIP from the aqueous phase and reaction with TMC molecules at the interface, fabricated CN interlayers were constructed to store and distribute PIP molecules more uniformly with limited access to the TMC

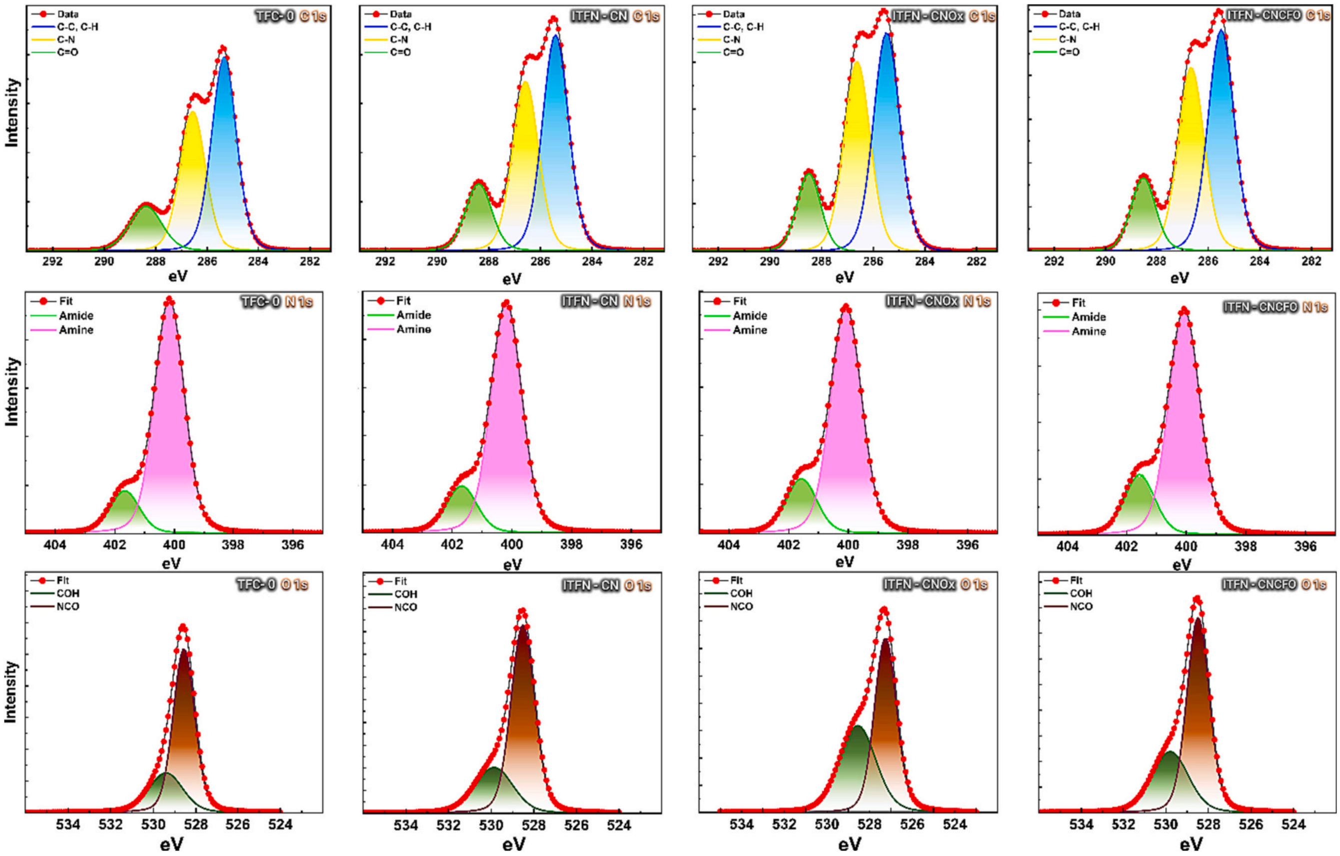

Fig. 5. High resolution XPS spectra of the prepared membranes.

[57]. More uniform and regulated release of PIP results in a thinner skin layer for ITFN membranes compared to TFC-0 (without interlayer) [55]. Due to their higher hydrophilicity and oxygen-containing functional groups, thinner polyamide layers are formed on ITFN-CNOx and ITFN-CNCFO membranes than on ITFN-CN membranes. Fig. 4c displays the 3D images and surface roughness for ITFN-CN, ITFN-CNOx, and ITFN-CNCFO membranes measured by AFM. SEM and AFM data corroborate the observation that ITFN-CN, ITFN-CNOx, and ITFN-CNFCO membranes had smoother surfaces than TFC-0. This may be explained by the smoother surface of the coated substrate and its higher surface wettability compared to the pristine PES substrate (without the interlayer). The uniform wetting of the PIP aqueous solution on the pristine PES substrate is not achieved to the same extent as on the coated substrates. Consequently, PIP diffuses unevenly during interfacial polymerization, resulting in a rougher polyamide layer for TFC-0 membranes than for ITFN membranes [58,59]. Moreover, as highlighted by Yang et al. [60], the incorporation of an interlayer can effectively decrease the rate of amine monomer release and slow down its diffusion. This phenomenon leads to the formation of thinner polyamide layers with smoother surface [61,62]. It is also possible that the roughness of the substrate modified with CNCFO nanosheets is responsible for the increased surface roughness of the ITFN-CNCFO membrane as compared to the ITFN-CN and ITFN-CNOx membranes (Fig. 3) [45]. The presence of $CuFe_2O_4$ particles on the CNCFO nanosheets, which impairs the directed stacking of CNCFO nanosheets during vacuum filtering, may explain this difference.

3.3. *Surface properties of membranes*

XPS measurements were conducted to investigate the elemental composition and chemical bonding of TFC-0, ITFN-CN, ITFN-CNOx, and ITFN-CNCFO membranes. Fig. 5 shows the XPS carbon (C 1s), (O 1s), and nitrogen (N 1s) spectra of the membranes. More detailed information including the atomic percentages of each element, O/N ratio, and degree of cross-linking of the membranes are provided in Table 2. Theoretical O/N ratios span a range from 1.0 (indicating 100 % cross-linking) in a fully cross-linked structure, where each oxygen atom is linked to a nitrogen atom through an amide bond, to 2.0 (indicating 0 % cross-linking) in a fully linear structure that incorporates additional oxygen atoms within unreacted carboxylic groups. By increasing the cross-linking degree of the polyamide, a denser polyamide structure is achieved, resulting in higher selectivity [63]. A crosslinking degree of the polyamide active layer for prepared membranes was calculated based on the O/N elemental ratio from the XPS spectra [64]. Table 2 shows that the degrees of crosslinking of polyamide active layer for ITFN membranes increased compared to the TFC-0 membrane, suggesting that the presence of interlayers increased the degree of crosslinking. The highly cross-linked networks of the ITFN membranes commonly resulted in a denser polyamide structure and thus higher rejections [65]. The difference in the degree of cross-linking of ITFN membranes may be explained by the functional groups of interlayers. These membrane interlayers have functional groups that promote the controlled release of

Table 2
Elemental composition, O/N ratio, and degree of cross-linking of the membranes.

Membrane	Atomic concentration (%)			O/N ratio	Degree of cross-linking (%)
	C (1s)	O (1s)	N (1s)		
TFC-0	73.05	12.75	9.17	1.39	51.0
ITFN-CN-25	72.75	13.71	11.62	1.18	74.0
ITFN-CNOx-25	72.18	14.82	12.89	1.15	79.1
ITFN-CNCFO-25	72.22	14.21	12.18	1.17	76.8

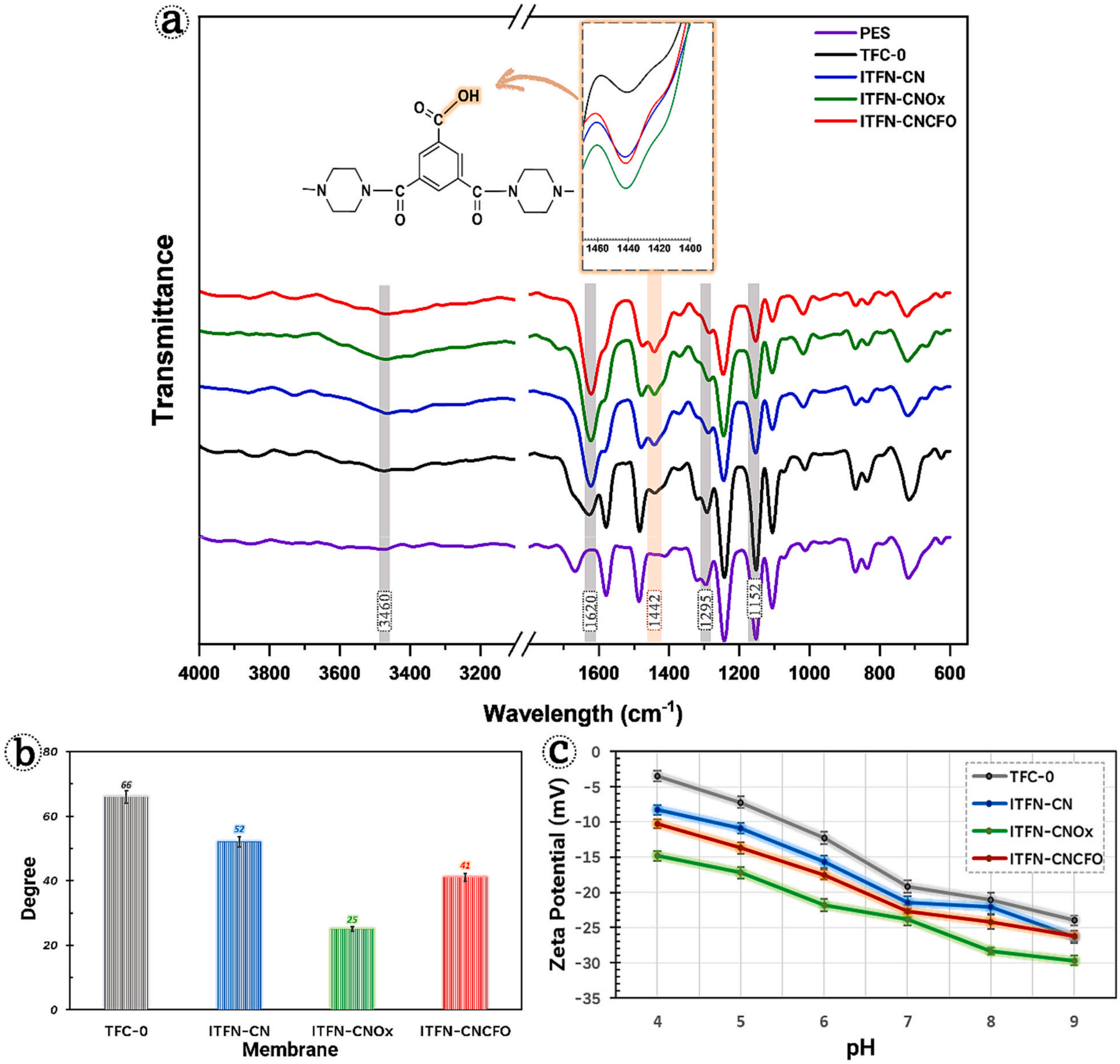

Fig. 6. FTIR spectra (a), water contact angle (b), and zeta potential (c) of the prepared membranes.

PIP molecules by hydrogen bonding with their amine groups. The more controllable release of PIP molecules from the aqueous phase to the interface leads to a more orderly manner reaction between PIP and TMC and reduced TMC consumption with a larger proportion of cross-linked structures [66]. The degree of cross-linking for the ITFN-CNOx membrane is slightly higher than for the ITFN-CNCFO membrane. The difference between the ITFN-CNCFO and ITFN-CNOx membranes may result from the reaction of some CNOx hydrophilic functional groups when it was decorated onto the copper ferrite ($CuFe_2O_4$) to form CNCFO. The surface of PES, TFC-0, ITFN-CN, ITFN-CNOx, and ITFN-CNCFO membranes was analyzed by FTIR-ATR (Fig. 6a). TFC-0, ITFN-CN, ITFN-CNOx, and ITFN-CNCFO membranes showed additional peaks at 1442 and 1625 cm^{-1} compared to the PES substrate. These peaks, belonging to OH bending vibrations and C═O stretching vibrations of amide groups in polyamide, show that the polyamide layer was formed by interfacial polymerization on the PES substrate [63]. The broad peak at 3450 cm^{-1} corresponds to the OH stretching of carboxylic groups, which were formed by hydrolysis of unreacted COCl groups. The C—C stretching vibration of aromatic rings is characterized by the peak at roughly 1485 cm^{-1} [67]. The peak at 1245 cm^{-1} corresponds to the asymmetric stretching vibration of C—O—C, and the peaks at 1295 cm^{-1} and 1152 cm^{-1} to the symmetric and asymmetric stretching vibrations of S═O from the PES substrate [63,68]. The intensified peak at 1442 cm^{-1} for ITFN-CNCFO corresponds to the OH stretching vibration of carboxyl groups [57]. The increased intensity of this peak can be attributed to the greater hydrolysis of acyl chloride groups in TMC, leading to the formation of additional carboxylic groups [69]. The higher cross-linked polyamide network would hinder the diffusion of PIP molecules more, leading to lower PIP content on the top surface of the nascent polyamide film. As a result, the hydrolysis of TMC would be enhanced [65,70]. With regard to degree of cross-linking of ITFN membranes, the peak intensity at 1442 cm^{-1} for the ITFN-CNCFO membrane is lower than for the ITFN-CNOx membrane and higher than for the ITFN-CN membrane. The evaluation of membrane surface hydrophilicity was performed through measurements of water contact angles, as illustrated in Fig. 6b. Incorporating interlayers increased the surface hydrophilicity of ITFN-CN, ITFN-CNOx, and ITFN-CNCFO, as shown by the reduction in their contact angles relative to the TFC-0 membrane. The increased hydrolysis of acyl chloride groups in TMC may account for some of its increased hydrophilicity [69]. An amplified peak at 1442 cm^{-1}, corresponding to

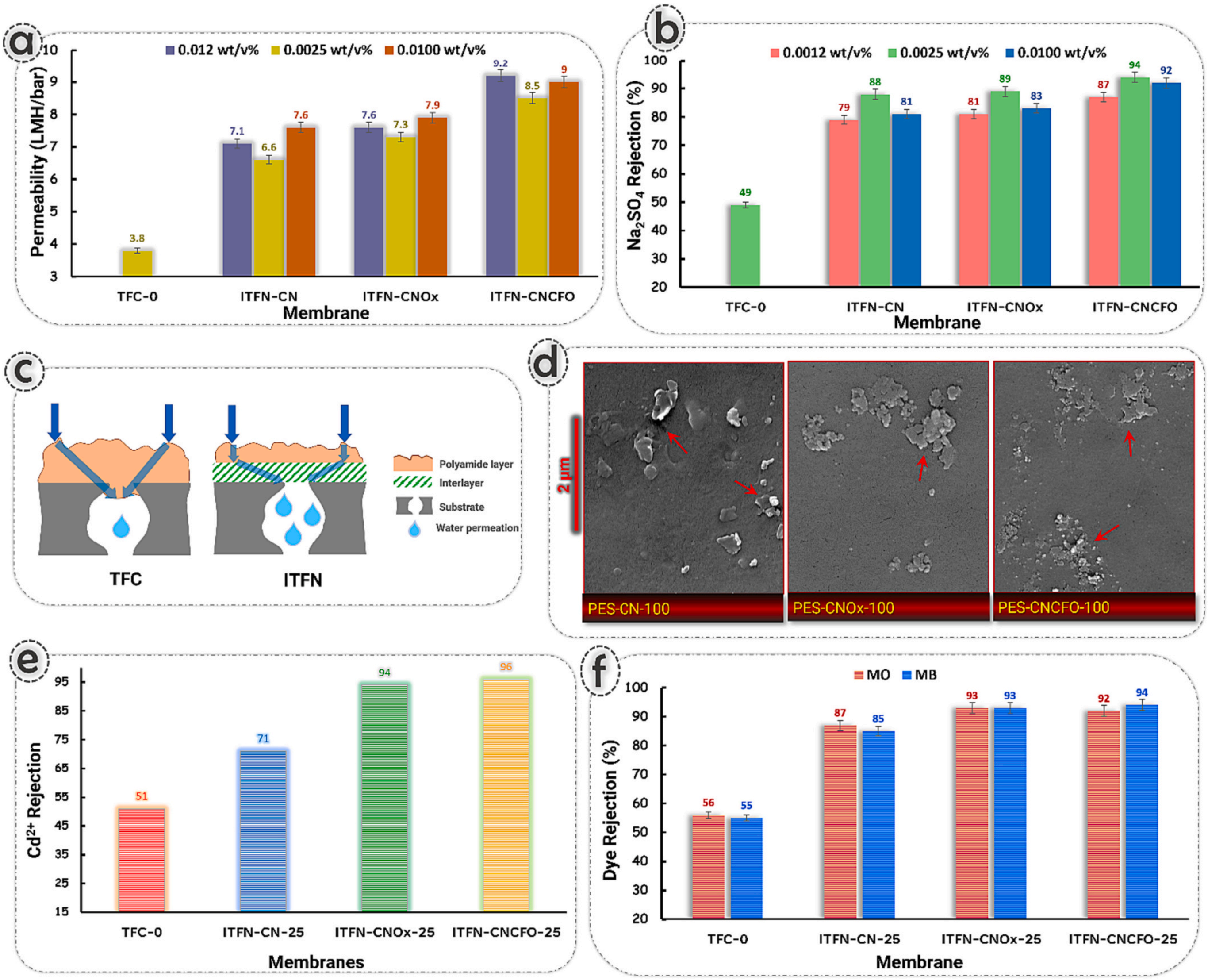

Fig. 7. Water permeability (a) and Na_2SO_4 rejection (b) of the prepared membranes. Mechanistic insights into the role of the interlayer; a schematic illustration (c) of the mechanisms (gutter effect) is provided to explain how this effect enhances the separation performance of the ITFN membranes. Reproduced with permission from [77]. In TFC membrane, the average transport path through the polyamide layer in TFC membrane is notably longer than the thickness of the polyamide layer. In contrast, ITN membranes exhibit a shorter path length for water transport through the less permeable polyamide layer resulting in a longer path through the more permeable interlayer. This configuration leads to a reduction in the overall hydraulic resistance of the membrane. The inhomogeneous formation of interlayer (d) at high loading amounts (0.0100 wt/v%) of interlayers. Cd^{2+} (e) and dye (f) rejection of the prepared membranes. Membrane performance was tested at a transmembrane pressure of 3 bar at 24 °C with a solution pH of 6–7.

the OH stretching vibration of carboxyl groups and more hydrophilic functional groups of the interlayer, provides further evidence for increased hydrolysis. The enhanced presence of oxygen-containing functional groups, namely carboxyl and hydroxyl groups, within the interlayer of the ITFN-CNOx membrane, coupled with a more extensively cross-linked PA layer, effectively suppresses the PIP diffusion effect. This suppression promotes a higher degree of acyl chloride group hydrolysis, a component found in TMC. Consequently, a larger proportion of acyl chloride is converted into hydrophilic carboxyl groups. This transformation is evidenced by a reduced water contact angle of 25° for the ITFN-CNOx membrane, a significant decrease when compared to the water contact angles of the ITFN-CN membrane (52°) and the ITFN-CNCFO membrane (41°). Hydrolysis of the acyl chloride groups may explain the difference in contact angle between ITFN-CNCFO and ITFN-CNOx. CNCFO nanosheets contain more functional groups than CN and CNCFO, making them more hydrophilic. Fig. 6c compares the zeta potentials of all membranes. The ITFN membranes had more negative surface charges than TFC-0 because more controllable release of PIP molecules and reduced TMC consumption result in more -COOH groups from hydrolysis of unreacted acyl chloride. The ITFN-CNOx membrane had a slightly more negative surface charge due to enhanced hydrolysis of acyl chloride into negatively charged carboxyl groups [71].

3.4. Filtration performance of NF membranes

Fig. 7a and b show that the presence of an interlayer greatly improves water permeability and Na_2SO_4 rejection of ITFN membranes. The permeability and Na_2SO_4 rejection of the ITFN-CNCFO-25 membrane increased by >50 %, to 8.5 LMH/bar and 94 %, respectively. The significant increase in permeability observed in the ITFN membranes, in comparison to the control membrane, can be attributed to two key factors. Firstly, the interlayer serves as a high-permeability gutter layer, directly improving the pathway for water transport. Secondly, the interlayer indirectly affects polyamide formation by facilitating the creation of a thinner PA active layer, preventing polyamide intrusion, and enhancing the hydrophilicity of the membrane surface. An illustration of the gutter effect enhancing permeability can be seen in Fig. 7c. The CN, CNOx, and CNCFO interlayers, in fact, have lower resistance and a much higher intrinsic water permeability than polyamide film. Thus, the gutter effect could potentially reduce the overall hydraulic resistance because it minimizes the transport path within the low-permeable polyamide layer [72,73]. The study aimed to investigate the effect of nanosheet loading on the performance of fabricated membranes and determine the optimum mass loadings of interlayers. To achieve this, testing the NF desalination performance of control TFC-0 and a series of ITFN-X-Y membranes with different mass loadings were conducted. Fig. 7b demonstrates the effect of interlayer mass loading on the separation performance of the fabricated membranes. By increasing the mass loading of interlayers from 0.0012 wt/v% to 0.0025 wt/v%, the water permeability of all three ITFN membranes (ITFN-CN-25, ITFN-CNOx-25, and ITFN-CNCFO-25) decreased, while Na_2SO_4 rejection elevated up. The reason for the reduced permeability could be attributed to the much thicker interlayer that is formed at higher mass loadings of CN, CNCOx, and CNCFO interlayers, thereby adding further resistance to mass transfer and impeding water permeation. The increased Na_2SO_4 rejection observed in the interphase-based membranes with interlayer coatings suggested an enhancement in their selectivity. Higher mass loadings of interlayer contributed to defect-free PA layer with higher degree cross-linking and resulted in the increment of steric hindrance [74]. However, with the further increase of the mass loadings for all interlayers from 0.0025 wt/v% to 0.0100 wt/v%, the active layer was negatively impacted, and the selectivity of the membranes was compromised, despite being more permeable and selective than the control TFC-0 membrane. This could be attributed to the minor defects within the PA active layer, resulting from excessive loading and inhomogeneous formation of interlayers at high concentrations, as well as rough interlayer surfaces (see Fig. 7d) [75]. The findings indicate that the optimum mass loading for the interlayers is 0.0025 wt/v%. This loading will be utilized to investigate separation performance and fouling behaviors of fabricated membranes (ITFN-X-25). At an interlayer mass loading of 0.0025 wt/v%, the ITFN-CN-25 membrane demonstrated a permeability of 6.6 LMH/bar (a 42 % increase compared to the TFC-0 membrane) and a Na_2SO_4 rejection of 88 %. Upon replacing the CN interlayer with CNCOx and CNCFO, the permeability of the ITFN-CNOx-25 and ITFN-CNCFO-25 membranes was further improved to 7.3 LMH/bar and 8.5 LMH/bar, respectively (a 48 % and 55 % increase compared to the TFC-0 membrane), while maintaining Na_2SO_4 rejection of 89 % and 94 %, respectively. The enhanced performance of the membrane can be mainly attributed to the presence of an oxidized region of nanosheets, which exhibit hydrophilic properties. This region plays a crucial role in improving the substrate's hydrophilicity, enabling greater storage capacity for aqueous monomer molecules, better regulation of their release, and the provision of additional channels that facilitate water permeation [58,73]. Compared with ITFN-CNOx, the slightly higher permeability of ITFN-CNCFO may be attributed to the larger interlayer spacing due to solid 3D $CuFe_2O_4$ decoration on CNCFO nanosheets, providing more water pathways [64,76]. Moreover, higher surface area owing to its rougher surface could also improve the water permeability of ITFN-CNCFO [77]. The slight difference in rejection of ITFN-CNOx and ITFN-CNFO membranes is in agreement with their respective surface characteristics. The surface of the ITFN-CNOx membrane has a higher concentration of hydrated acyl chloride groups than the ITFN-CNCFO membrane. This increased concentration of functional groups leads to a decrease in sieving efficiency and, consequently, slightly lower sieving ability. These findings are in agreement with previous research [10]. The rejection rates for Cadmium ion (Cd^{2+}) across the four different membranes are graphically represented in Fig. 7e. The inconsistency of the Donnan repulsion effect in rejecting Cd^{2+} cations indicates that size exclusion must be the primary rejection mechanism. Among the membranes tested, the ITFN-CN-25 membrane demonstrated a rejection rate of 71 %, which is significantly higher than the 51 % rejection rate observed for the TFC-0 membrane. Additionally, the ITFN-CNOx-25 and ITFN-CNCFO-25 membranes exhibited significantly higher rejection rates, with values of 94 % and 96 % respectively. This translates to an increase of >84 % and 88 % respectively, when compared to the bare TFC-0 membrane. These results underscore the significant enhancements in Cd^{2+} ion rejection capabilities brought about by the modifications in these membranes. This data offers valuable insights into the potential of these membranes for efficient cadmium ion rejection in water purification applications. Fig. 7f shows that the ITFN membranes removed organic dyes (MB and MO) more effectively than the bare TFC-0 membrane. The MB rejection rates were 55 % for TFC-0, 85 % for ITFN-CN-25, 93 % for ITFN-CNOx-25, and 94 % for ITFN-CNCFO-25. A similar trend was observed for MO rejection rates: 56 %, 87, 93 %, and 92 %. The removal efficiency of the ITFN membranes was almost the same for positively charged MB molecules and negatively charged MO molecules. Therefore, physical size sieving and steric factors are likely to contribute to the separation performance of these membranes [66,78]. In Table 3, we have provided a comparative analysis of the performance of our top-performing membrane, ITFNCNFO-25, with a selection of highly rated commercial NF membranes, as well as several NF membranes with and without interlayer documented in academic literature. Compared with most of other membranes, the membrane fabricated in this research exhibited superior pure water permeability while maintaining comparable rejection to other nanofiltration membranes, particularly commercially available ones. The $g-C_3N_4/CuFe_2O_4$ -interlayered TFN membrane (ITFNCNFO-25) developed in this study demonstrated excellent separation performances, with a water permeability of 8.5 LMH/bar and a Na_2SO_4 rejection of 94 %, surpassing the majority of other membranes listed in Table 3. Furthermore, the ITFNCNFO-25 membrane demonstrated significantly improved separation performance in terms of both water permeability and rejection compared to the control TFC-0 membrane without an interlayer. This indicates the membrane's promising potential for applications in the treatment of heavy metal wastewater and desalination processes. It is worth mentioning that our work utilized graphitic carbon nitride derivatives and its nanocomposites as an interphase layer in the fabrication of TNF membrane for the first time.

Table 3
Comparison of our best membrane with other NF membranes.

Membrane	Membrane type	Water flux (LMH/bar)	Na_2SO_4 rejection (%)	Ref
PEI-TMC/PDA/PAN	TFC	2.1	92.4	[79]
PA/COFs/PSF HF	TFN	8.66	96.6	[80]
PA/GO/PSF HF	TFN	8.39	96.10	[81]
PA/PDA-COF/PAN	TFC	20.7	93.4	[82]
PA/salt modified/PES	TFC	5.1	60	[83]
PA/MWCNT-NH/PSF	TFC	5.3	96.8	[84]
Poly (aryl cyanurate)/PES	TFC	1.7	97.1	[5]
NF270	Commercial	13.1	98.1	[85]
NF90	Commercial	6.7	98.6	[85]
AMS (A3012)	Commercial	2.1	∼95	[86]
Nadir (NP030P)	Commercial	>1.0	80–95	[86–89]
SUEZ (Duracid)	Commercial	1.1–1.3	∼98	[86]
SUEZ (HL)	Commercial	5.5	_	[4]
Synder (NDX)	Commercial	9.8	_	[4]
TriSep (TS80)	Commercial	4.3	_	[90]
Osmonics (Desal 5DK)	Commercial	3.6–4.5	96.8	[91]
ITFNCNFO-25	TFN	8.5	94	This work

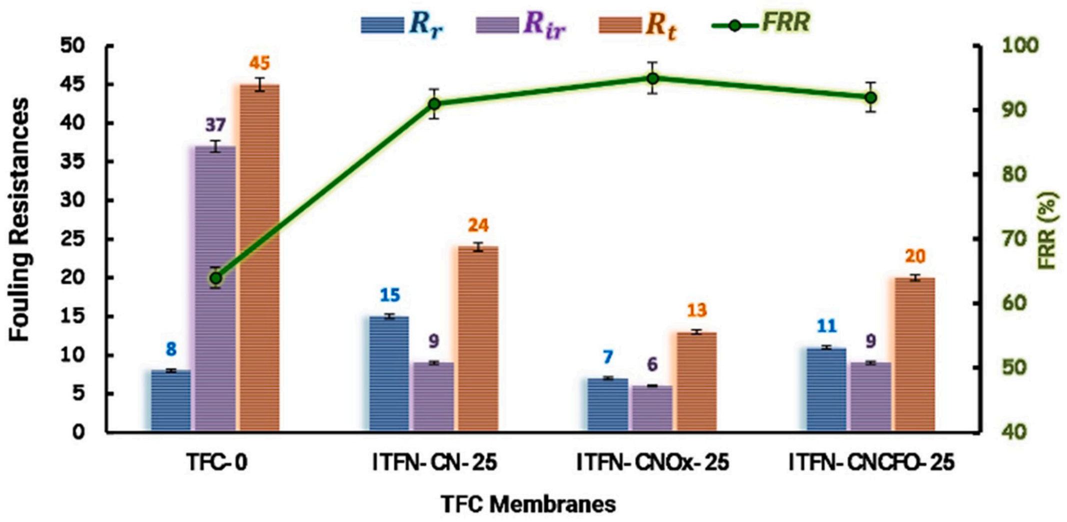

Fig. 8. The fouling resistances and flux recovery ratio of the prepared membranes.

3.5. Antifouling assessment of the membrane

The accumulation of organic and inorganic foulants on the surfaces of membranes lowers their nanofiltration efficiency and lifetime [27]. Fouling is mainly affected by membrane roughness, surface charge, and hydrophilicity [4,92]. Hydrophobic interactions can facilitate the adsorption of organic foulants on nanofiltration membranes [93], while water molecules form a protective layer on hydrophilic surfaces, preventing foulants from adhering to them [94]. Negatively charged membranes are less prone to fouling by most contaminants that are also negatively charged in water due to electrostatic repulsion. Finally, foulants can more easily adhere to the valleys of rough surfaces, where there is less water mixing [95,96].

The fouling resistance of the ITFN membranes was assessed through filtration experiments using a BSA solution. Fig. 8 compares the flux recovery ratio (FRR), reversible fouling resistance (R_r), flux loss due to irreversible fouling (R_{ir}), and total flux decline ratio (R_t). The nanosheet interlayers increased the FRR of all ITFN membranes: 91 % for ITFN- CN-25, 95 % for ITFN-CNOx-25, and 92 % for ITFN-CNCFO-25, in contrast to only 64 % for the TFC-0 membrane. The lower hydrophilicity and rougher surface of the TFC-0 membrane made it easier for BSA to adsorb to its surface, and harder to wash it off [97]. ITFN-CNOx-25 was more hydrophilic than ITFN-CN-25 and ITFN-CNCFO-25 (Fig. 6b), with a contact angle of 25°. The AFM images in Fig. 4c showed that the ITFN-CNCOx-25 membrane also had the lowest surface roughness ($R_a = 5.7$ nm) of all the interlayered membranes. Fig. 8 also shows that the ITFN membranes also had lower R_t and higher FRR values than the TFC-0 membrane. These findings prove that the ITFN-CNOx-25 and ITFN-CNCFO-25 membranes were harder to foul with BSA than the TFC-0 membrane. The improved organic fouling resistance of the membranes is attributed to their smoother surface and increased hydrophilicity [97,98]. The surface of the interlayered membrane adsorbs more water molecules and generates a dense hydration layer, which ultimately prevents the adsorption of contaminants on the membrane surface [2].

4. Conclusion

Interlayered thin film nanocomposite (ITFN) membranes were synthesized by incorporating graphitic carbon nitride (g-C_3N_4; CN), oxidized g-C_3N_4 (CNCOx) and g-C_3N_4/$CuFe_2O_4$ (CNCFO) nanosheets on the surface of a PES substrate using vacuum filtration, then conducting interfacial polymerization of PIP and TMC on the interlayers. The interlayers greatly helped to tune the thickness, surface roughness, and zeta potential of the polyamide active layer, boosting both the permeability and rejection of the resulting nanofiltration membranes.

The permeability of the ITFN membrane with the optimum content of CNCFO (about 8.5 LMH/bar) was more than two times that of the control membrane (TFC-0). The interlayer was conducive to the preparation of a tuned polyamide rejection layer with more cross-linking and negative charge by regulating the IP reaction, which in turn afforded the ITFN-CNCFO-25 membrane rejections of 94 %, 92 %, 96 %, and 94 % for MB, MO, Cd^{2+}, and Na_2SO_4, respectively. Finally, ITFN membranes drastically showed improved antifouling and enhanced flux recovery ratio (FRR) for nanofiltration separations, thanks to the improved surface properties controlling the deposition and adsorption of foulants on the membrane surface. This research provides a novel route to make high-performance ITFN NF membranes through designing a multifunctional interlayer using carbon nitride 2D nanosheets.

Declaration of competing interest

The authors declare that they have no known competing financial interests or personal relationships that could have appeared to influence the work reported in this paper.

Data availability

Data will be made available on request.

Acknowledgment

The financial support for this work by the Natural Sciences and Engineering Research Council of Canada (NSERC), Canada's Oil Sands Innovation Alliance (COSIA) and Lorestan University is gratefully acknowledged. S.A.A. acknowledges the financial support provided by the Killam Centre for Advanced Studies through the Izaak Walton Killam Memorial Scholarship, as well as the Alberta Innovates Graduate Student Scholarship (AIGSS), sponsored by Alberta Innovates of the Alberta government, Canada.

Appendix A. Supplementary data

Supplementary data to this article can be found online at https://doi.org/10.1016/j.jwpe.2023.104432.

References

[1] S. Kamari, A. Shahbazi, Biocompatible Fe3O4@ SiO2-NH2 nanocomposite as a green nanofiller embedded in PES–nanofiltration membrane matrix for salts, heavy metal ion and dye removal: long–term operation and reusability tests, Chemosphere 243 (2020), 125282.

[2] G.A. Mulungulungu, T. Mao, K. Han, Two-dimensional graphitic carbon nitride-based membranes for filtration process: progresses and challenges, Chem. Eng. J. 427 (2022), 130955.

[3] Y. Mansourpanah, S.S. Madaeni, A. Rahimpour, A. Farhadian, The effect of non-contact heating (microwave irradiation) and contact heating (annealing process) on properties and performance of polyethersulfone nanofiltration membranes, Appl. Surf. Sci. 255 (2009) 8395–8402.

[4] A. Asad, S.A. Aktij, P. Karami, D. Sameoto, M. Sadrzadeh, Micropatterned thin-film composite poly (piperazine-amide) nanofiltration membranes for wastewater treatment, ACS Appl. Polym. Mater. 3 (2021) 6653–6665.

[5] M.G. Elshof, E. Maaskant, M.A. Hempenius, N.E. Benes, Poly (aryl cyanurate)-based thin-film composite nanofiltration membranes, ACS Appl. Polym. Mater. 3 (2021) 2385–2392.

[6] Y. Yang, L. Yu, T. Chu, H. Niu, J. Wang, Y. Cai, Constructing chemical stable 4-carboxyl-quinoline linked covalent organic frameworks via Doebner reaction for nanofiltration, Nat. Commun. 13 (2022) 1–9.

[7] A.A. Tashvigh, T.-S. Chung, Facile fabrication of solvent resistant thin film composite membranes by interfacial crosslinking reaction between polyethylenimine and dibromo-p-xylene on polybenzimidazole substrates, J. Membr. Sci. 560 (2018) 115–124.

[8] S.M. Nejad, S.F. Seyedpour, S.A. Aktij, M.D. Firouzjaei, M. Elliott, A. Tiraferri, M. Sadrzadeh, A. Rahimpour, Loose nanofiltration membranes functionalized with in situ-synthesized metal organic framework for water treatment, Mater. Today Chem. 24 (2022), 100909.

[9] Y. Mansourpanah, A. Ghanbari, H. Yazdani, A.G. Mohammadi, A. Rahimpour, Silver-polyamidoamine/graphene oxide thin film nanofiltration membrane with improved antifouling and antibacterial properties for water purification and desalination, Desalination 511 (2021), 115109.

[10] S. Xue, C.-W. Lin, C. Ji, Y. Guo, L. Liu, Z. Yang, S. Zhao, X. Cai, Q.J. Niu, R.B. Kaner, Thin-film composite membranes with a hybrid dimensional titania interlayer for ultrapermeable nanofiltration, Nano Lett. 22 (2022) 1039–1046.

[11] L. Ma, Q. Bi, Y. Tang, C. Zhang, F. Qi, H. Zhang, Y. Gao, S. Xu, Fabrication of high-performance nanofiltration membrane using polydopamine and carbon nitride as the interlayer, Separations 9 (2022) 180.

[12] Y. Liang, C. Li, S. Li, B. Su, M.Z. Hu, X. Gao, C. Gao, Graphene quantum dots (GQDs)-polyethyleneimine as interlayer for the fabrication of high performance organic solvent nanofiltration (OSN) membranes, Chem. Eng. J. 380 (2020), 122462.

[13] W.-J. Lau, G.-S. Lai, J. Li, S. Gray, Y. Hu, N. Misdan, P.-S. Goh, T. Matsuura, I. W. Azelee, A.F. Ismail, Development of microporous substrates of polyamide thin film composite membranes for pressure-driven and osmotically-driven membrane processes: a review, J. Ind. Eng. Chem. 77 (2019) 25–59.

[14] Y. Wang, B. Gao, Q. Yue, Z. Wang, Graphitic carbon nitride (gC 3 N 4)-based membranes for advanced separation, J. Mater. Chem. A Mater. 8 (2020) 19133–19155.

[15] F. Yang, G. Ding, J. Wang, Z. Liang, B. Gao, M. Dou, C. Xu, S. Li, Self-cleaning, antimicrobial, and antifouling membrane via integrating mesoporous graphitic carbon nitride into polyvinylidene fluoride, J. Membr. Sci. 606 (2020), 118146.

[16] Q. Bi, C. Zhang, J. Liu, Q. Cheng, S. Xu, A nanofiltration membrane prepared by PDA-C3N4 for removal of divalent ions, Water Sci. Technol. 81 (2020) 253–264.

[17] Y. Deng, J. Zhang, Q. Li, T. Liu, Y. Yang, Highly chlorine-oxidation and fouling resistant thin film nanocomposite membrane enhanced by few-layered graphitic carbon nitride nanosheets, Environ Sci.: Water Res. Technol. 8 (2022) 1976–1991.

[18] Y. Mansourpanah, MXenes and other 2D nanosheets for modification of polyamide thin film nanocomposite membranes for desalination, Sep. Purif. Technol. 120777 (2022).

[19] Y. Zhou, Y. Wu, H. Wu, J. Xue, L. Ding, R. Wang, H. Wang, Fast hydrogen purification through graphitic carbon nitride nanosheet membranes, Nat. Commun. 13 (2022) 1–10.

[20] L. Long, C. Wu, Z. Yang, C.Y. Tang, Carbon nanotube interlayer enhances water permeance and antifouling performance of nanofiltration membranes: mechanisms and experimental evidence, Environ. Sci. Technol. 56 (2022) 2656–2664.

[21] L. Ma, Q. Bi, W. Zhou, X. Liu, F. Qi, H. Zhang, Y. Gao, S. Xu, Nanofiltration membrane with a zwitterion-g-C3N4 composite interlayer for Mg2+/Li+ separation, J. Water Process Eng. 53 (2023), 103751.

[22] L. Gui, Y. Cui, Y. Zhu, X. An, H. Lan, J. Jin, g-C3N4 nanofibers network reinforced polyamide nanofiltration membrane for fast desalination, Sep. Purif. Technol. 293 (2022), 121125.

[23] W.-T. Lin, C.-Y. Zhu, D. Zhou, W.-L. Li, P. Fu, X.-J. Huang, Z.-K. Xu, L.-S. Wan, Functionalized g-C3N4 nanosheet interlayer enables enhanced separation performance of nanofiltration membranes, Sep. Purif. Technol. 324 (2023), 124543.

[24] B. Ma, G. Chen, C. Fave, L. Chen, R. Kuriki, K. Maeda, O. Ishitani, T.-C. Lau, J. Bonin, M. Robert, Efficient visible-light-driven CO2 reduction by a cobalt molecular catalyst covalently linked to mesoporous carbon nitride, J. Am. Chem. Soc. 142 (2020) 6188–6195.

[25] J.Y. Shen, Z.S. Cui, Z.W. Wu, J.X. Wang, Q. Ning, X.M. Lü, Simple preparation of CuFe2O4/C3N4 composites: characterisation and enhanced photocatalysis, Mater. Res. Innov. 19 (2015) 187–191.

[26] M.D. Firouzjaei, M. Pejman, M.S. Gh, S.A. Aktij, E. Zolghadr, A. Rahimpour, M. Sadrzadeh, A.A. Shamsabadi, A. Tiraferri, M. Elliott, Functionalized polyamide membranes yield suppression of biofilm and planktonic bacteria while retaining flux and selectivity, Sep. Purif. Technol. 282 (2022), 119981.

[27] S.A. Aktij, A. Rahimpour, A. Figoli, Low content nano-polyrhodanine modified polysulfone membranes with superior properties and their performance for wastewater treatment, Environ. Sci. Nano 4 (2017) 2043–2054.

[28] M.-B. Wu, Y. Lv, H.-C. Yang, L.-F. Liu, X. Zhang, Z.-K. Xu, Thin film composite membranes combining carbon nanotube intermediate layer and microfiltration support for high nanofiltration performances, J. Membr. Sci. 515 (2016) 238–244.

[29] M. Chi, P. Zheng, M. Wei, A. Zhu, L. Zhong, Q. Zhang, Q. Liu, Polyamide composite nanofiltration membrane modified by nanoporous TiO2 interlayer for enhanced water permeability, J. Ind. Eng. Chem. 115 (2022) 230–240.

[30] J.-J. Wang, H.-C. Yang, M.-B. Wu, X. Zhang, Z.-K. Xu, Nanofiltration membranes with cellulose nanocrystals as an interlayer for unprecedented performance, J. Mater. Chem. A Mater. 5 (2017) 16289–16295.

[31] H. Jafarian, M.D. Firouzjaei, S.A. Aktij, A. Aghaei, M.P. Khomami, M. Elliott, E. K. Wujcik, M. Sadrzadeh, A. Rahimpour, Synthesis of heterogeneous metal organic framework-graphene oxide nanocomposite membranes for water treatment, Chem. Eng. J. 455 (2023), 140851.

[32] M. Mazani, S. Aghapour Aktij, A. Rahimpour, N. Tavajohi Hassan Kiadeh, Cu-BTC metal− organic framework modified membranes for landfill leachate treatment, Water (Basel) 12 (2019) 91.

[33] E. Coppini, L. Palli, D. Fibbi, R. Gori, Long-term performance of a full-scale membrane plant for landfill leachate pretreatment: a case study, Membranes (Basel) 8 (2018) 52.

[34] S. Kang, L. Zhang, M. He, Y. Zheng, L. Cui, D. Sun, B. Hu, "Alternated cooling and heating" strategy enables rapid fabrication of highly-crystalline g-C3N4 nanosheets for efficient photocatalytic water purification under visible light irradiation, Carbon N.Y. 137 (2018) 19–30.

[35] M.R. Esfahani, S.A. Aktij, Z. Dabaghian, M.D. Firouzjaei, A. Rahimpour, J. Eke, I. C. Escobar, M. Abolhassani, L.F. Greenlee, A.R. Esfahani, Nanocomposite membranes for water separation and purification: fabrication, modification, and applications, Sep. Purif. Technol. 213 (2019) 465–499.

[36] H.-J. Li, B.-W. Sun, L. Sui, D.-J. Qian, M. Chen, Preparation of water-dispersible porous gC 3 N 4 with improved photocatalytic activity by chemical oxidation, Phys. Chem. Chem. Phys. 17 (2015) 3309–3315.

[37] F. Dong, Z. Zhao, T. Xiong, Z. Ni, W. Zhang, Y. Sun, W.-K. Ho, In situ construction of g-C3N4/g-C3N4 metal-free heterojunction for enhanced visible-light photocatalysis, ACS Appl. Mater. Interfaces 5 (2013) 11392–11401.

[38] K. Pandiselvi, H. Fang, X. Huang, J. Wang, X. Xu, T. Li, Constructing a novel carbon nitride/polyaniline/ZnO ternary heterostructure with enhanced photocatalytic performance using exfoliated carbon nitride nanosheets as supports, J. Hazard. Mater. 314 (2016) 67–77.

[39] Z. Zhu, X. Tang, C. Ma, M. Song, N. Gao, Y. Wang, P. Huo, Z. Lu, Y. Yan, Fabrication of conductive and high-dispersed Ppy@ Ag/g-C3N4 composite photocatalysts for removing various pollutants in water, Appl. Surf. Sci. 387 (2016) 366–374.

[40] R. Kumar, M.A. Barakat, F.A. Alseroury, Oxidized g-C3N4/polyaniline nanofiber composite for the selective removal of hexavalent chromium, Sci. Rep. 7 (2017) 1–11.

[41] X. Chen, Y.-S. Jun, K. Takanabe, K. Maeda, K. Domen, X. Fu, M. Antonietti, X. Wang, Ordered mesoporous SBA-15 type graphitic carbon nitride: a semiconductor host structure for photocatalytic hydrogen evolution with visible light, Chem. Mater. 21 (2009) 4093–4095.

[42] D.L. Pavia, G.M. Lampman, G.S. Kriz, J.A. Vyvyan, Introduction to Spectroscopy, Cengage learning, 2014.

[43] C. Nethravathi, M. Rajamathi, Chemically modified graphene sheets produced by the solvothermal reduction of colloidal dispersions of graphite oxide, Carbon N.Y. 46 (2008) 1994–1998.

[44] L. Qi, J. Yu, M. Jaroniec, Preparation and enhanced visible-light photocatalytic H 2-production activity of CdS-sensitized Pt/TiO 2 nanosheets with exposed (001) facets, Phys. Chem. Chem. Phys. 13 (2011) 8915–8923.

[45] L. Nalbandian, E. Patrikiadou, V. Zaspalis, A. Patrikidou, E. Hatzidaki, C. N. Papandreou, Magnetic nanoparticles in medical diagnostic applications: synthesis, characterization and proteins conjugation, Curr. Nanosci. 12 (2016) 455–468.

[46] X. Wang, K. Maeda, A. Thomas, K. Takanabe, G. Xin, J.M. Carlsson, K. Domen, M. Antonietti, A metal-free polymeric photocatalyst for hydrogen production from water under visible light, Nat. Mater. 8 (2009) 76–80.

[47] A.W. Burton, K. Ong, T. Rea, I.Y. Chan, On the estimation of average crystallite size of zeolites from the Scherrer equation: a critical evaluation of its application to zeolites with one-dimensional pore systems, Microporous Mesoporous Mater. 117 (2009) 75–90.

[48] J. Xu, L. Zhang, R. Shi, Y. Zhu, Chemical exfoliation of graphitic carbon nitride for efficient heterogeneous photocatalysis, J. Mater. Chem. A Mater. 1 (2013) 14766–14772.

[49] S. Arunvisut, S. Phummanee, A. Somwangthanaroj, Effect of clay on mechanical and gas barrier properties of blown film LDPE/clay nanocomposites, J. Appl. Polym. Sci. 106 (2007) 2210–2217.

[50] S. Xia, M. Ni, T. Zhu, Y. Zhao, N. Li, Ultrathin graphene oxide nanosheet membranes with various d-spacing assembled using the pressure-assisted filtration method for removing natural organic matter, Desalination 371 (2015) 78–87.

[51] P. Niu, L. Zhang, G. Liu, H. Cheng, Graphene-like carbon nitride nanosheets for improved photocatalytic activities, Adv. Funct. Mater. 22 (2012) 4763–4770.

[52] Y. Yao, F. Lu, Y. Zhu, F. Wei, X. Liu, C. Lian, S. Wang, Magnetic core–shell CuFe2O4@ C3N4 hybrids for visible light photocatalysis of Orange II, J. Hazard. Mater. 297 (2015) 224–233.

[53] S. Shao, F. Zeng, L. Long, X. Zhu, L.E. Peng, F. Wang, Z. Yang, C.Y. Tang, Nanofiltration membranes with crumpled polyamide films: a critical review on mechanisms, performances, and environmental applications, Environ. Sci. Technol. 56 (2022) 12811–12827.

[54] B. Khorshidi, T. Thundat, B.A. Fleck, M. Sadrzadeh, A novel approach toward fabrication of high performance thin film composite polyamide membranes, Sci. Rep. 6 (2016) 1–10.

[55] J. Zhang, S. Li, D. Ren, H. Li, X. Lv, L. Han, B. Su, Fabrication of ultra-smooth thin-film composite nanofiltration membrane with enhanced selectivity and permeability on interlayer of hybrid polyvinyl alcohol and graphene oxide, Sep. Purif. Technol. 268 (2021), 118649.

[56] Z. Liu, Z. An, Z. Mi, Z. Wang, Q. Zhu, D. Zhang, J. Wang, J. Liu, J. Zhang, Thin-film composite nanofiltration membranes with poly (amidoxime) as organic interlayer for effective desalination, J. Environ. Chem. Eng. 10 (2022), 107015.

[57] X. Yang, Controllable interfacial polymerization for nanofiltration membrane performance improvement by the polyphenol interlayer, ACS Omega 4 (2019) 13824–13833.

[58] Y. Li, Y. Su, J. Li, X. Zhao, R. Zhang, X. Fan, J. Zhu, Y. Ma, Y. Liu, Z. Jiang, Preparation of thin film composite nanofiltration membrane with improved structural stability through the mediation of polydopamine, J. Membr. Sci. 476 (2015) 10–19.

[59] X. Zhang, Y. Lv, H.-C. Yang, Y. Du, Z.-K. Xu, Polyphenol coating as an interlayer for thin-film composite membranes with enhanced nanofiltration performance, ACS Appl. Mater. Interfaces 8 (2016) 32512–32519.

[60] Z. Yang, P.-F. Sun, X. Li, B. Gan, L. Wang, X. Song, H.-D. Park, C.Y. Tang, A critical review on thin-film nanocomposite membranes with interlayered structure: mechanisms, recent developments, and environmental applications, Environ. Sci. Technol. 54 (2020) 15563–15583.

[61] W. Choi, S. Jeon, S.J. Kwon, H. Park, Y.-I. Park, S.-E. Nam, P.S. Lee, J.S. Lee, J. Choi, S. Hong, Thin film composite reverse osmosis membranes prepared via layered interfacial polymerization, J. Membr. Sci. 527 (2017) 121–128.

[62] S. Karan, Z. Jiang, A.G. Livingston, Sub–10 nm polyamide nanofilms with ultrafast solvent transport for molecular separation, Science 348 (2015) (1979) 1347–1351.

[63] A. Rahimpour, S.F. Seyedpour, S. Aghapour Aktij, M. Dadashi Firouzjaei, A. Zirehpour, A. Arabi Shamsabadi, S. Khoshhal Salestan, M. Jabbari, M. Soroush, Simultaneous improvement of antimicrobial, antifouling, and transport properties of forward osmosis membranes with immobilized highly-compatible polyrhodanine nanoparticles, Environ. Sci. Technol. 52 (2018), https://doi.org/10.1021/acs.est.8b00804.

[64] Z. Wang, Z. Wang, S. Lin, H. Jin, S. Gao, Y. Zhu, J. Jin, Nanoparticle-templated nanofiltration membranes for ultrahigh performance desalination, Nat. Commun. 9 (2018) 1–9.

[65] X. Zhu, X. Cheng, X. Luo, Y. Liu, D. Xu, X. Tang, Z. Gan, L. Yang, G. Li, H. Liang, Ultrathin thin-film composite polyamide membranes constructed on hydrophilic poly (vinyl alcohol) decorated support toward enhanced nanofiltration performance, Environ. Sci. Technol. 54 (2020) 6365–6374.

[66] L. Chen, N. Li, Z. Wen, L. Zhang, Q. Chen, L. Chen, P. Si, J. Feng, Y. Li, J. Lou, Graphene oxide based membrane intercalated by nanoparticles for high performance nanofiltration application, Chem. Eng. J. 347 (2018) 12–18.

[67] A. Rahimpour, M. Jahanshahi, A. Mollahosseini, B. Rajaeian, Structural and performance properties of UV-assisted TiO2 deposited nano-composite PVDF/SPES membranes, Desalination 285 (2012) 31–38.

[68] M. Peyravi, A. Rahimpour, M. Jahanshahi, A. Javadi, A. Shockravi, Tailoring the surface properties of PES ultrafiltration membranes to reduce the fouling resistance using synthesized hydrophilic copolymer, Microporous Mesoporous Mater. 160 (2012) 114–125.

[69] Z. Yang, Z. Zhou, H. Guo, Z. Yao, X. Ma, X. Song, S.-P. Feng, C.Y. Tang, Tannic acid/Fe3+ nanoscaffold for interfacial polymerization: toward enhanced nanofiltration performance, Environ. Sci. Technol. 52 (2018) 9341–9349.

[70] C. Jiang, L. Tian, Z. Zhai, Y. Shen, W. Dong, M. He, Y. Hou, Q.J. Niu, Thin-film composite membranes with aqueous template-induced surface nanostructures for enhanced nanofiltration, J. Membr. Sci. 589 (2019), 117244.

[71] Z. Yao, Z. Yang, H. Guo, X. Ma, Y. Dong, C.Y. Tang, Highly permeable and highly selective ultrathin film composite polyamide membranes reinforced by reactable polymer chains, J. Colloid Interface Sci. 552 (2019) 418–425.

[72] B. Yuan, S. Zhao, P. Hu, J. Cui, Q.J. Niu, Asymmetric polyamide nanofilms with highly ordered nanovoids for water purification, Nat. Commun. 11 (2020) 1–12.

[73] L. Gui, J. Dong, W. Fang, S. Zhang, K. Zhou, Y. Zhu, Y. Zhang, J. Jin, Ultrafast ion sieving from honeycomb-like polyamide membranes formed using porous protein assemblies, Nano Lett. 20 (2020) 5821–5829.

[74] N.S. Suhalim, N. Kasim, E. Mahmoudi, I.J. Shamsudin, A.W. Mohammad, F. Mohamed Zuki, N.L.-A. Jamari, Rejection mechanism of ionic solute removal by nanofiltration membranes: an overview, Nanomaterials 12 (2022) 437.

[75] Z. Zhang, X. Shi, R. Wang, A. Xiao, Y. Wang, Ultra-permeable polyamide membranes harvested by covalent organic framework nanofiber scaffolds: a two-in-one strategy, Chem. Sci. 10 (2019) 9077–9083.

[76] X. Wu, M. Ding, H. Xu, W. Yang, K. Zhang, H. Tian, H. Wang, Z. Xie, Scalable ti3c2t x mxene interlayered forward osmosis membranes for enhanced water purification and organic solvent recovery, ACS Nano 14 (2020) 9125–9135.

[77] Z. Yang, F. Wang, H. Guo, L.E. Peng, X. Ma, X. Song, Z. Wang, C.Y. Tang, Mechanistic insights into the role of polydopamine interlayer toward improved separation performance of polyamide nanofiltration membranes, Environ. Sci. Technol. 54 (2020) 11611–11621.

[78] L. Chen, Y. Li, L. Chen, N. Li, C. Dong, Q. Chen, B. Liu, Q. Ai, P. Si, J. Feng, A large-area free-standing graphene oxide multilayer membrane with high stability for nanofiltration applications, Chem. Eng. J. 345 (2018) 536–544.

[79] Z. Yang, X. Huang, J. Wang, C.Y. Tang, Novel polyethyleneimine/TMC-based nanofiltration membrane prepared on a polydopamine coated substrate, Front. Chem. Sci. Eng. 12 (2018) 273–282.

[80] Y. Jiang, S. Li, J. Su, X. Lv, S. Liu, B. Su, Two dimensional COFs as ultra-thin interlayer to build TFN hollow fiber nanofiltration membrane for desalination and heavy metal wastewater treatment, J. Membr. Sci. 635 (2021), 119523.

[81] L. Tian, Y. Jiang, S. Li, L. Han, B. Su, Graphene oxide interlayered thin-film nanocomposite hollow fiber nanofiltration membranes with enhanced aqueous electrolyte separation performance, Sep. Purif. Technol. 248 (2020), 117153.

[82] M. Wu, J. Yuan, H. Wu, Y. Su, H. Yang, X. You, R. Zhang, X. He, N.A. Khan, R. Kasher, Ultrathin nanofiltration membrane with polydopamine-covalent organic framework interlayer for enhanced permeability and structural stability, J. Membr. Sci. 576 (2019) 131–141.

[83] J. Xiang, Z. Xie, M. Hoang, K. Zhang, Effect of amine salt surfactants on the performance of thin film composite poly (piperazine-amide) nanofiltration membranes, Desalination 315 (2013) 156–163.

[84] S.-M. Xue, Z.-L. Xu, Y.-J. Tang, C.-H. Ji, Polypiperazine-amide nanofiltration membrane modified by different functionalized multiwalled carbon nanotubes (MWCNTs), ACS Appl. Mater. Interfaces 8 (2016) 19135–19144.

[85] C. Liu, L. Shi, R. Wang, Crosslinked layer-by-layer polyelectrolyte nanofiltration hollow fiber membrane for low-pressure water softening with the presence of SO42− in feed water, J. Membr. Sci. 486 (2015) 169–176.

[86] L. Yu, K. Li, Y. Zhang, J. Wang, G. Zhang, Improved permeability of tight acid resistant nanofiltration membrane via citric acid post-treatment, J. Membr. Sci. 648 (2022), 120381.

[87] Y. Mansourpanah, H.S. Afarani, K. Alizadeh, M. Tabatabaei, Enhancing the performance and antifouling properties of nanoporous PES membranes using microwave-assisted grafting of chitosan, Desalination 322 (2013) 60–68.

[88] C.Y. Tang, Y.-N. Kwon, J.O. Leckie, Probing the nano-and micro-scales of reverse osmosis membranes—a comprehensive characterization of physiochemical properties of uncoated and coated membranes by XPS, TEM, ATR-FTIR, and streaming potential measurements, J. Membr. Sci. 287 (2007) 146–156.

[89] T. Yun, J.W. Chung, S.-Y. Kwak, Recovery of sulfuric acid aqueous solution from copper-refining sulfuric acid wastewater using nanofiltration membrane process, J. Environ. Manag. 223 (2018) 652–657.

[90] H. Zhang, Q. He, J. Luo, Y. Wan, S.B. Darling, Sharpening nanofiltration: strategies for enhanced membrane selectivity, ACS Appl. Mater. Interfaces 12 (2020) 39948–39966.

[91] A. Akbari, J.C. Remigy, P. Aptel, Treatment of textile dye effluent using a polyamide-based nanofiltration membrane, Chem. Eng. Process. Process Intensif. 41 (2002) 601–609.

[92] Y. Han, Y. Jiang, C. Gao, High-flux graphene oxide nanofiltration membrane intercalated by carbon nanotubes, ACS Appl. Mater. Interfaces 7 (2015) 8147–8155.

[93] S. Zinadini, A.A. Zinatizadeh, M. Rahimi, V. Vatanpour, H. Zangeneh, Preparation of a novel antifouling mixed matrix PES membrane by embedding graphene oxide nanoplates, J. Membr. Sci. 453 (2014) 292–301.

[94] P. Karami, S.A. Aktij, B. Khorshidi, M.D. Firouzjaei, A. Asad, M. Elliott, A. Rahimpour, J.B.P. Soares, M. Sadrzadeh, Nanodiamond-decorated thin film composite membranes with antifouling and antibacterial properties, Desalination 522 (2022), 115436.

[95] M. Hayatbakhsh, M. Sadrzadeh, D. Pernitsky, S. Bhattacharjee, J. Hajinasiri, Treatment of an in situ oil sands produced water by polymeric membranes, Desalin. Water Treat. 57 (2016) 14869–14887.

[96] M. Sadrzadeh, J. Hajinasiri, S. Bhattacharjee, D. Pernitsky, Nanofiltration of oil sands boiler feed water: effect of pH on water flux and organic and dissolved solid rejection, Sep. Purif. Technol. 141 (2015) 339–353.

[97] G.S. Lai, W.J. Lau, P.S. Goh, Y.H. Tan, B.C. Ng, A.F. Ismail, A novel interfacial polymerization approach towards synthesis of graphene oxide-incorporated thin film nanocomposite membrane with improved surface properties, Arab. J. Chem. 12 (2019) 75–87.

[98] H.M. Hegab, Y. Wimalasiri, M. Ginic-Markovic, L. Zou, Improving the fouling resistance of brackish water membranes via surface modification with graphene oxide functionalized chitosan, Desalination 365 (2015) 99–107.